Nano Research

Open Access

Research Article

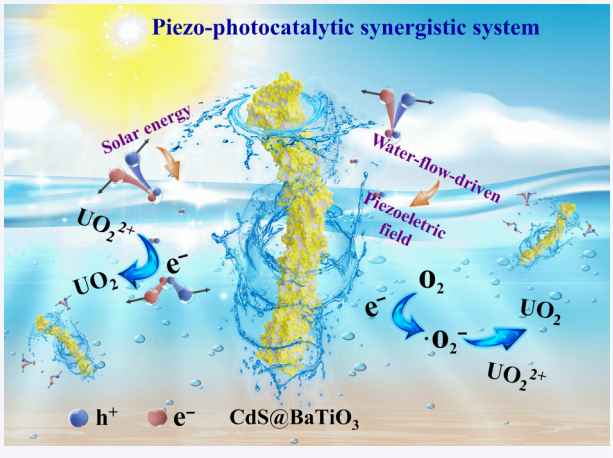
Piezo-photocatalytic synergistic reduction of U(VI) over $CdS@BaTiO_3$ heterostructure composites

Teng He[1,2], Yanxin Jiang[2,3], Wei Wang[4], Jingjing Wang[1] ✉, Peng Liu[5], Ping Li[2,3,6] ✉, Duoqiang Pan[1] ✉, and Qiaohui Fan[2,3]

[1] *State Key Laboratory of Chemistry for NBC Hazards Protection, Frontiers Science Center for RareIsotopes, School of Nuclear Science and Technology, Lanzhou University, Lanzhou 730000, China*
[2] *State Key Laboratory of Cryospheric Science and Frozen Soil Engineering, Northwest Institute of Eco-Environment and Resources, Chinese Academy of Sciences, Lanzhou 730000, China*
[3] *Key Laboratory of Petroleum Resources Exploration and Evaluation, Northwest Institute of Eco-Environment and Resources, Chinese Academy of Sciences, Lanzhou 730000, China*
[4] *Hangzhou Customs Technology Center, Hangzhou 311215, China*
[5] *Yantai Research Institute, Harbin Engineering University, Yantai 264000, China*
[6] *Changyi Marine Ecology and Engineering Research Station, Northwest Institute of Eco-Environment and Resources, Chinese Academy of Sciences, Changyi 261300, China*

Cite this article: *Nano Research*, **2026**, *19*, 94908657. https://doi.org/10.26599/NR.2026.94908657

ABSTRACT: Photocatalytic separation of uranium presents a promising approach for resource recovery, yet its efficiency remains limited by severe charge-carrier recombination. Integrating piezocatalysis with photocatalysis offers an attractive pathway to overcome this barrier. Herein, a Type-II $CdS@BaTiO_3$ heterojunction was fabricated by growing CdS nanoparticles onto a $BaTiO_3$ matrix, which enables efficient piezo-photocatalytic uranium extraction. The built-in electric field of the heterojunction, reinforced by the stirring-induced piezoelectric polarization of $CdS@BaTiO_3$, drives directional charge migration and greatly enhances carrier separation. As a result, $CdS@BaTiO_3$ achieved 98% uranium removal within 10 min under stirring and light irradiation, which was 2.5 and 8.3 times higher than those achieved by photocatalysis and piezocatalysis alone, respectively. The composite also delivers a high uranium separation capacity of 1893.2 $mg \cdot g^{-1}$, exceeding most previously reported piezo-photocatalytic uranium extraction systems. Mechanistic investigations identify superoxide radicals ($\cdot O_2^-$) as the dominant reactive species responsible for U(VI) reduction and immobilization. This work demonstrates a promising water-flow-driven energy-coupling strategy for uranium extraction.



KEYWORDS: piezo-photocatalysis, uranium extraction, heterojunction, reduction

1 Introduction

As a sustainable and renewable energy source, nuclear power is increasingly recognized as a viable alternative to conventional fossil fuels [1]. Uranium is the primary raw material for nuclear power generation, and the growing global energy demand has further intensified the urgency for its efficient utilization [2]. However, uranium mining and processing generate large amounts of uranium-containing wastewater, leading to the wastage of recoverable uranium resources and posing serious environmental risks [3, 4]. From the perspective of resource utilization and environmental sustainability, uranium recovery from contaminated radioactive wastewater is of paramount importance [5]. Currently, photocatalytic uranium separation has shown good promise owing to its eco-friendliness and sustainability [6–8]. Nevertheless, its practical application remains limited by the poor photoconversion

Received: December 17, 2025; **Revised:** February 9, 2026
Accepted: March 21, 2026

✉Address correspondence to Jingjing Wang, wangjj@nwpu.edu.cn; Ping Li, liping@lzb.ac.cn; Duoqiang Pan, panduoqiang@lzu.edu.cn

efficiency and low separation efficiency of photogenerated electron–hole pairs. Therefore, exploring new strategies to achieve efficient uranium separation and recovery is urgently required.

Constructing an internal electric field (IEF) is an effective strategy for regulating the separation of photoexcited charge carriers [9, 10]. Notably, piezocatalysis is able to harvest mechanical energy from fluid motion, stirring, ultrasound, or ball milling to generate an internal polarization field, thereby facilitating charge separation and redox reactions [11, 12]. Moreover, ubiquitous mechanical forces in natural environments, such as friction, wind, and tides, can be exploited to regulate the polarization intensity [13]. However, most reported piezocatalysts are highly dependent on ultrasonic excitation via the cavitation effect to trigger piezocatalytic reactions [14]. Correspondingly, almost all relevant studies on piezocatalytic uranium separation to date were conducted exclusively through ultrasonication. Nevertheless, ultrasonication inevitably brings high noise pollution and energy consumption, making it energy-inefficient and impractical for large-scale applications [15, 16]. In addition, ultrasound may induce micro-pitting on the catalyst surface, weaken the interfacial contact between composite components, and thus limit material lifetime [17, 18]. In comparison, stirring provides the lowest energy consumption and simplest operational mode [13]. The shear force generated during stirring induces deformation in the piezoelectric material, creating a continuous unidirectional piezoelectric field with easily tunable stirring rate and direction [19]. Moreover, stirring delivers a low-frequency and low-energy input that preserves the structural integrity and reusability of materials. Previous studies have validated that piezoelectric field created by stirring can modulate the charge transfer behavior [20]. Benefiting from these advantages, constructing built-in electric fields by stirring offers an attractive pathway to enhance the performance of traditional photocatalysts [21].

Recently, the representative ferroelectric material barium titanate ($BaTiO_3$) has attracted considerable attention owing to its noncentrosymmetric perovskite structure, which endows it with high dielectric permittivity and piezoelectric coefficient [22]. The piezocatalytic activity of $BaTiO_3$ is closely associated with its intrinsic piezoelectric properties and morphology. Low-dimensional (one-dimensional (1D) and two-dimensional (2D)) nanostructures (e.g., nanorod) exhibit higher mechanical energy harvesting and piezoelectric response, owing to their small Young's modulus and high deformability [20, 23]. To further enhance photocatalytic efficiency, heterojunction engineering has been introduced to accelerate the migration and separation of photogenerated charge carriers [24, 25]. Cadmium sulfide (CdS), with its narrow band gap and suitable conduction band (CB) position, exhibits good photocatalytic activity and intrinsic piezoelectric property [26, 27]. Combining $BaTiO_3$ with CdS enables the construction of a heterojunction with optimized band alignment for redox reactions [28]. Moreover, the polarization field generated by the piezoelectric response, together with the built-in field at the heterojunction interface, jointly accelerates charge separation and transfer, delivering a pronounced synergistic effect in the piezo-assisted photocatalytic system [15, 29].

Building on the above insights, this study proposes a stir-induced piezo-photocatalyst strategy, in which a novel Type-II-scheme CdS@$BaTiO_3$ heterojunction was constructed for efficient uranium separation. The catalytic activity of CdS@$BaTiO_3$ towards U(VI) was systematically evaluated under combined piezocatalytic and photocatalytic conditions, specifically focusing on how the heterojunction architecture and piezoelectric properties affect the photocatalytic performance. The results showed that the piezo-polarized field promoted efficient interfacial charge transfer, and the uranium separation was significantly improved through the synergistic interaction between the built-in electric field and the piezoelectric field. Remarkably, the CdS@$BaTiO_3$ system achieved outstanding uranium separation efficiency (99.8%) within 10 min without the use of any sacrificial agents. Detailed analyses regarding potential reaction pathways and uranium transformation processes were also systematically clarified. This work thus presents a practical approach for the stirring-induced piezo-photocatalytic extraction of uranium from water.

2 Experimental

2.1 Preparation of $BaTiO_3$ nanorods

$BaTiO_3$ nanorods were obtained via hydrothermal synthesis. Briefly, 1.25 g TiO_2 was dispersed in 60 mL 10 M NaOH aqueous solution, followed by magnetic stirring for 90 min and sonication for 60 min. The mixed solution was heated at 200 °C for 24 h, followed by filtration, washing, and drying of the obtained product. Subsequently, the produced sodium trititanate ($Na_2Ti_3O_7$) was added to 0.2 M HCl solution and stirred for 4 h to prepare titanic acid ($H_2Ti_3O_7$). Thereafter, 0.95 g $Ba(OH)_2{\cdot}8H_2O$ and 0.15 g $H_2Ti_3O_7$ were mixed with 60 mL purified water. The mixture was ultrasonicated for 30 min and was heated at 200 °C for 8 h. The product was then collected, washed, and dried. The resulting white product was named $BaTiO_3$.

2.2 Preparation of CdS@$BaTiO_3$ nanoparticles

CdS@$BaTiO_3$ heterojunctions were hydrothermally synthesized. Specifically, 10 mg of $Cd(CH_3COO)_2{\cdot}2H_2O$ was dissolved in 10 mL of ethanol, 0.05 g of $BaTiO_3$ was subsequently added, followed by ultrasonication for 30 min and heating at 80 °C for 10 min (Solution A). Meanwhile, 3 mg of thioacetamide (TAA) was dissolved in 10 mL deionized water to prepare Solution B. Under rapid magnetic stirring, the above-prepared Solution B was added dropwise to Solution A. Subsequently, the mixture solution was heated at 80 °C for 30 min. After natural cooling to ambient temperature, the final precipitates were filtered and collected. The obtained product was denoted as the CdS@$BaTiO_3$ heterojunction. CdS was prepared using the same method in the absence of $BaTiO_3$. The preparation diagram of CdS@$BaTiO_3$ is shown in Fig. 1(a).

2.3 Catalytic reactions for U(VI)

The catalytic performance was tested in a 25 mL quartz reactor. In the experiment, 4 mg of catalyst, 0.375 mL U(VI) solution (4 mM), and 14.625 mL of deionized water were added to the reactor. Prior to the catalytic procedure, the suspension was equilibrated in darkness for 30 min. During the experiments, piezocatalytic, photocatalytic, and piezo-photocatalytic reactions were performed under magnetic stirring (1500 rpm), visible light irradaition (500 W Xe lamp), and combined stirring-light conditions, respectively. Nitrogen gas was continuously purged throughout the reaction to maintain an inert atmosphere. At regular intervals, 0.5 mL of sample was collected and analyzed using an ultraviolet–visible (UV–Vis) spectrophotometer to monitor U(VI) concentration. The uranium removal capacity of the catalyst was evaluated by

sequentially adding 0.1 mol·L^{-1} uranium solution to the reaction system after each reaction stage. The process was repeated multiple times, allowing the catalyst to progressively accumulate uranium from the solution until no further removal was observed. After completion of the reaction, the samples were collected, washed, and then reused to evaluate material stability. The desorption process was performed using 0.1 M Na_2CO_3.

2.4 Characterization

Details were given in the Electronic Supplementary Material (ESM).

3 Results and discussion

3.1 Structural analysis of catalysts

The morphologies of the prepared $BaTiO_3$ and $CdS@BaTiO_3$ were characterized by scanning electron microscopy (SEM), transmission electron microscopy (TEM), and high-resolution TEM (HRTEM). The SEM (Fig. 1(b)) and TEM (Fig. 1(d)) images show that pure $BaTiO_3$ has a homogeneous and dispersed nanorod structure, and the average diameter of nanorods was 150–200 nm. Long $BaTiO_3$ nanorods offer higher surface area and more active sites, and the inherent transverse quantum confinement allows electrons to transfer directionally along the one-dimensional axis, enhancing charge carrier localization [30–32]. HRTEM image (Fig. 1(f)) reveals that the lattice fringes of the nanorods exhibit interplanar spacings of approximately 0.28 and 0.23 nm, which correspond to the (110) and the (111) planes of $BaTiO_3$ (PDF#01-085-0368). For $CdS@BaTiO_3$ (Figs. 1(c) and 1(e)), the nanorod substrate surface became coarse and uniformly dispersed with small-sized irregular-shaped nanoparticles. This is mainly because the $BaTiO_3$ surface acts as nucleation sites, facilitating the formation and growth of CdS

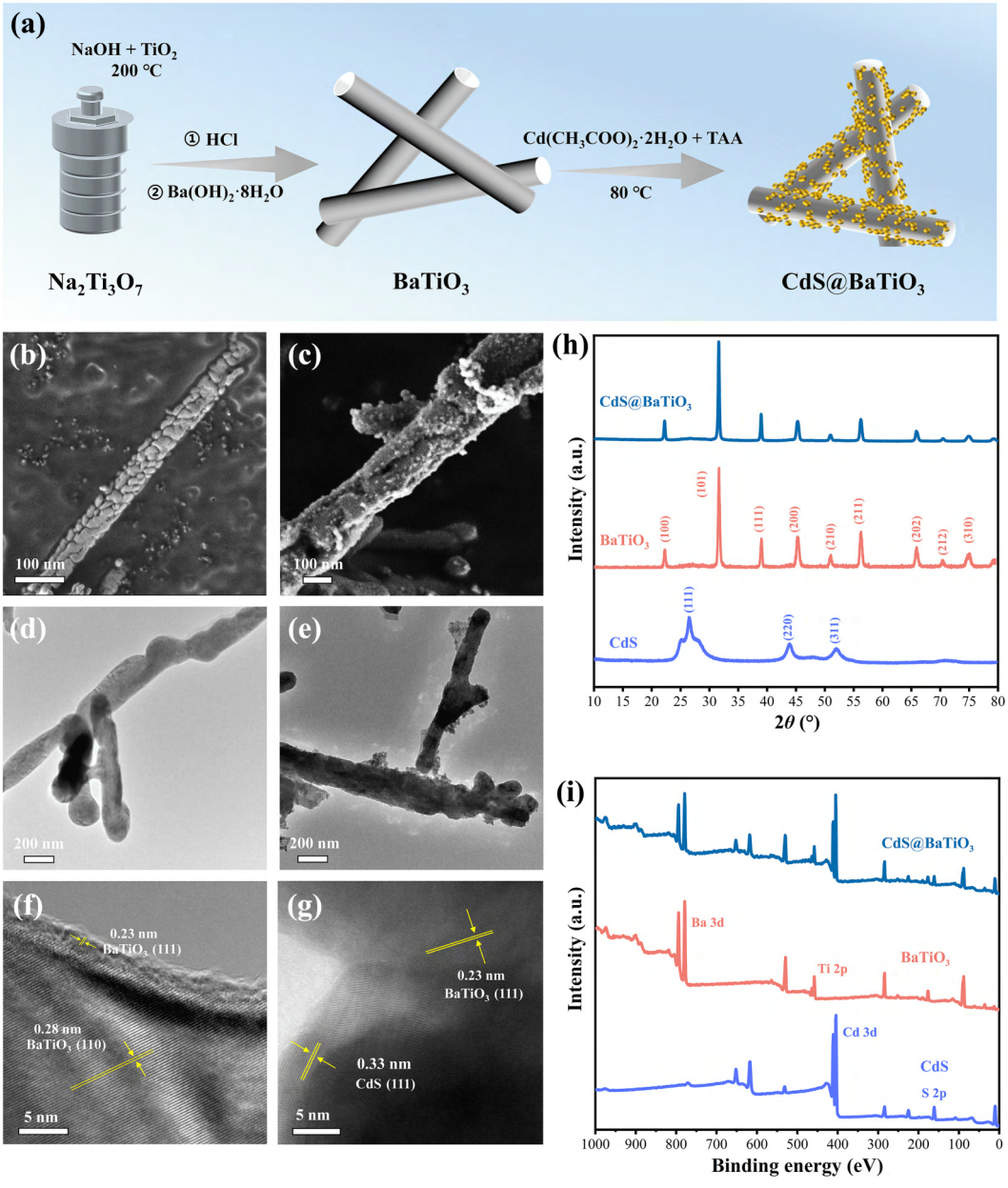


Figure 1 (a) The synthetic route of $CdS@BaTiO_3$ composite. (b) SEM, (d) TEM, and (f) HRTEM images of $BaTiO_3$. (c) SEM, (e) TEM, and (g) HRTEM images of $CdS@BaTiO_3$. (h) XRD patterns and (i) XPS survey spectra of CdS, $BaTiO_3$, and $CdS@BaTiO_3$.

nanocrystals. The corresponding HRTEM (Fig. 1(g)) image highlights the distinguishable hetero-interface between $BaTiO_3$ and CdS, with a lattice spacing of 0.33 nm consistent with the (111) plane of CdS (PDF#00-041-1049), indicative of successful deposition of CdS.

Crystalline and phase structures of $BaTiO_3$, CdS, and CdS@$BaTiO_3$ composites were characterized by X-ray diffraction (XRD) measurements, as shown in Fig. 1(h). The diffraction peaks of $BaTiO_3$ at 2θ values of 22.18°, 31.60°, 38.99°, 45.28°, 50.96°, 56.29°, 65.90°, 70.46°, and 74.95° well correspond to the (100), (110), (111), (200), (210), (211), (220), (221), and (310) planes of PDF#01-085-0368, respectively. The main characteristic peaks of pure CdS can be clearly observed, indicative of the hexagonal wurtzite CdS phase (PDF#00-041-1049) [33]. Several weak and broad diffraction peaks originate from the fragmentary growth of CdS nanostructures, revealing the aggregation of small, poorly crystalline, or ultrathin CdS particles [34]. For CdS@$BaTiO_3$, these diffraction peaks exhibit similarity to the crystallinity of CdS [35]. The element compositions and orthorhombic phase of $BaTiO_3$, with no distinct characteristic peaks of CdS observed due to low amount and poor chemical states, were explored by X-ray photoelectron spectroscopy (XPS), which showed that CdS@$BaTiO_3$ is composed of Ba, Ti, O, Cd, and S elements (Fig. 1(i)). In Fig. S1(a) in the ESM, the high-resolution Cd 3d spectrum of CdS presents two peaks at 411.8 eV ($3d_{3/2}$) and 405.1 eV ($3d_{5/2}$), respectively. The two S 2p peaks (Fig. S1(b) in the ESM) were observed at 162.5 eV ($2p_{1/2}$) and 161.3 eV ($2p_{3/2}$), respectively. As shown in the Ba 3d spectra (Fig. S1(c) in the ESM), the characteristic peaks at 795.4 and 793.9 eV corresponded to Ba $3d_{3/2}$, while the peaks at 780.1 and 778.6 eV were attributed to Ba $3d_{5/2}$. In Ti 2p spectra (Fig. S1(d) in the ESM), the characteristic signals located at 463.8 and 458.0 eV could be indexed as Ti $2p_{1/2}$ and Ti $2p_{3/2}$, respectively [22], conforming to the typical characteristics of Ti(IV).

Notably, compared to CdS and $BaTiO_3$, the Cd 3d and S 2p peaks of CdS@$BaTiO_3$ shifted to lower binding energy, while the Ba 3d and Ti 2p peaks of CdS@$BaTiO_3$ shifted to higher binding energy, reflecting the strong charge redistribution between $BaTiO_3$ and CdS. Meanwhile, this demonstrates interfacial coupling of $BaTiO_3$ and CdS and the formation of CdS@$BaTiO_3$ heterojunction. Specifically, the electrons are transferred from $BaTiO_3$ to interfaced CdS in CdS@$BaTiO_3$, and the charge-transfer path is consistent with a Type-II mechanism [36]. Therefore, the results demonstrate the successful preparation of CdS@$BaTiO_3$.

3.2 Piezoelectric and photoelectrochemical properties

External stress on piezoelectric materials induces charge center asymmetry that generates a polarization field [37]. The piezoelectric characteristics of $BaTiO_3$, CdS, and CdS@$BaTiO_3$ were examined using piezoresponse force microscopy (PFM). From the surface topography images (Fig. S2 in the ESM), the catalysts exhibit irregular grain sizes and a rough, uneven surface. The amplitude (Figs. 2(a), 2(d), and 2(g)) and phase (Figs. 2(b), 2(e), and 2(h)) of the piezoresponse reveal the piezoelectric potential and phase difference, confirming that $BaTiO_3$, CdS, and CdS@$BaTiO_3$ possess piezoelectric properties. Under a direct current (DC) bias field of ±10 V, characteristic butterfly-shaped and 180° reversed piezoelectric hysteresis loops were revealed (Figs. 2(c), 2(f), and 2(i)). Moreover, the piezoelectric constant (d_{33}) values (Fig. S3 in the ESM) of CdS@$BaTiO_3$, CdS, and $BaTiO_3$ are calculated to be 27.99, 11.22, and 12.36 pm·V^{-1}, respectively. These results demonstrate that the piezoresponse of CdS@$BaTiO_3$ is much stronger than that of pure CdS and $BaTiO_3$, confirming its highest piezoelectric performance.

The optical absorption properties of the catalysts were investigated by UV/Vis diffuse reflectance spectroscopy (DRS). In Fig. 3(a), CdS exhibited the strongest light-harvesting capability among all samples. By contrast, CdS@$BaTiO_3$ showed an absorption intensity between that of $BaTiO_3$ and CdS, while preserving the characteristic spectral signatures of both components, indicating its hybridized optical structure. A similar trend is observed in the electrochemical impedance spectroscopy (EIS) Nyquist plots (Fig. 3(b)), where CdS@$BaTiO_3$ showed intermediate impedance behavior between $BaTiO_3$ and CdS. Despite exhibiting intermediate absorption and impedance characteristics, CdS@$BaTiO_3$ shows the lowest fluorescence intensity in the photoluminescence (PL) spectra (Fig. 3(c)), demonstrating the most efficient charge-carrier separation. From the Mott–Schottky (MS) plots, all three catalysts exhibited positive slopes (Fig. S4 in the ESM), confirming their n-type semiconductors [38]. According to the Tauc plots (Eq. (S1) in the ESM), the band gap of $BaTiO_3$ and CdS was estimated at 2.98 and 1.90 eV, respectively (Fig. 3(e)). The valence-band XPS spectra showed that the valence band (VB) maxima of $BaTiO_3$ and CdS were located at 1.59 and 1.92 eV, respectively (Fig. 3(f)). According to Eq. (S2) in the ESM, the corresponding VB edge potentials (E_{VB}) were calculated to be 1.15 and 1.48 V vs. normal hydrogen electrode (NHE), respectively. Therefore, the CB edge potential (E_{CB}) values for $BaTiO_3$ and CdS were calculated to be −1.83 and −0.42 V vs. NHE, respectively (Eq. (S3) in the ESM), theoretically meeting the requirements for U(VI) reduction (Fig. 3(g)).

The current responses of $BaTiO_3$, CdS, and CdS@$BaTiO_3$ were further evaluated under stirring, light irradiation, and combined stirring-light conditions. As shown in Fig. 3(d), magnetic stirring of these materials generated piezo-current, attributed to water-vortex-driven mechanical deformation of the catalyst particles [39]. Further, the piezoelectric current was positively correlated with stirring speed, with faster stirring generating higher transient piezoelectric responses (2500 rpm > 1500 rpm > 500 rpm, Fig. S3 in the ESM). Increasing stirring speed intensified mechanical stress and deformation of catalysts, resulting in a stronger piezoelectric potential [40] and enhanced carrier migration to the catalyst surface [41]. For all samples, the photocurrent was much higher than the piezo-current, indicating that both CdS and $BaTiO_3$ are more sensitive to light excitation than to external mechanical stress. Moreover, CdS exhibited stronger photo- and piezo-current responses than $BaTiO_3$, reflecting its higher intrinsic photocatalytic activity and piezoelectric sensitivity. After coupling the two components, the heterojunction exhibited further enhanced current output, demonstrating accelerated carrier generation and separation. Under simultaneous stirring and light irradiation, CdS@$BaTiO_3$ showed the highest current intensity among all samples, confirming the synergistic enhancement derived from the coupling of photo- and piezoelectric fields. In contrast, $BaTiO_3$ exhibited smaller current enhancement under stirring-light conditions. This is likely due to its low piezoelectric coefficient, which tends to provide an internal polarized electric field [42].

3.3 Piezo-photocatalytic U(VI) reduction performance

The piezo-photocatalytic U(VI) experiment setup is shown in Fig. 4(a). To optimize the system, we synthesized various

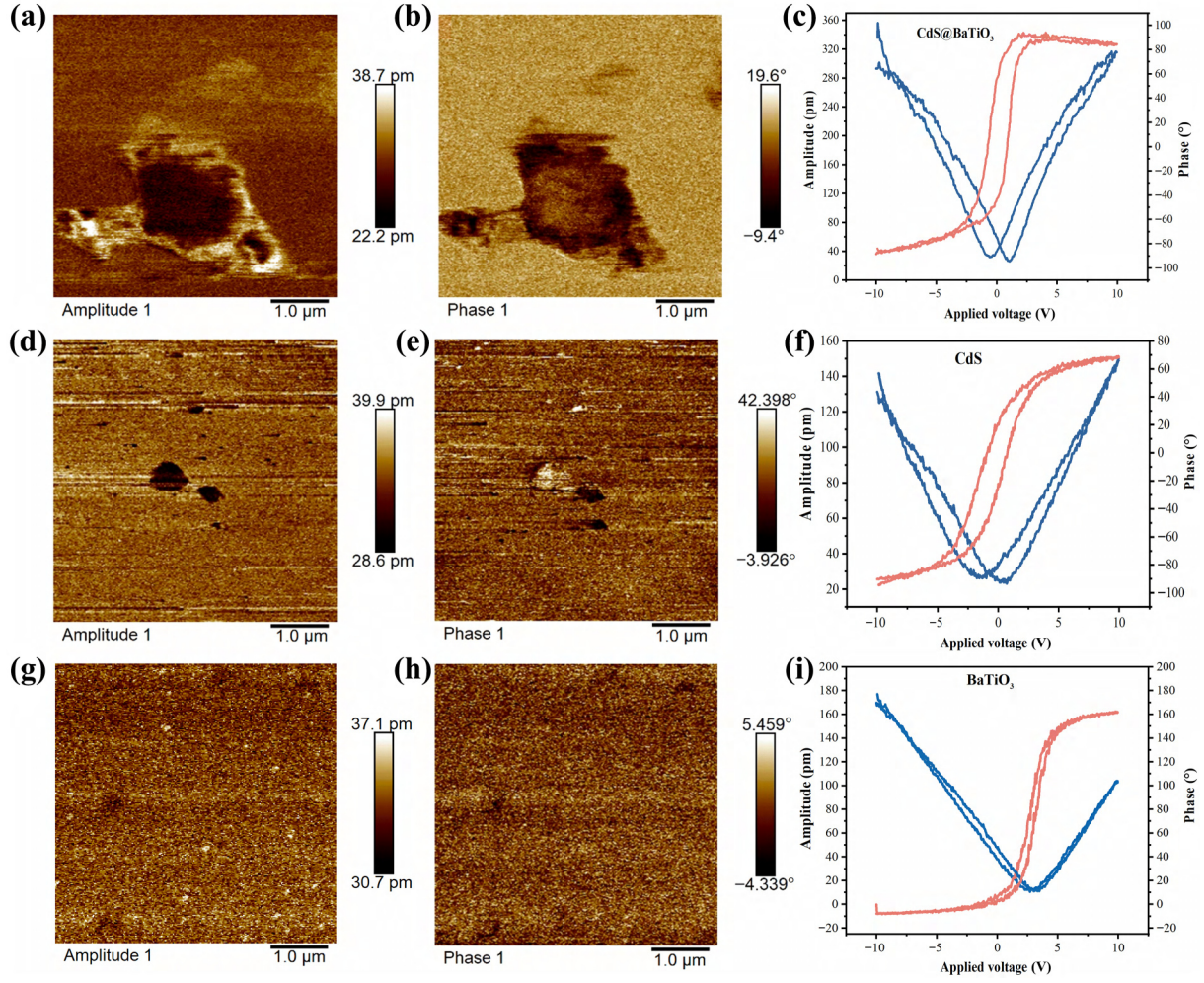


Figure 2 PFM images of $CdS@BaTiO_3$, CdS, and $BaTiO_3$. ((a), (d), and (g)) Amplitude images, ((b), (e), and (h)) phase images, and ((c), (f), and (i)) corresponding amplitude and phase curves.

$CdS@BaTiO_3$ materials with different ratios and tested their performance (Fig. S6 in the ESM). The 2:1 $BaTiO_3$ to CdS ratio was selected for further investigations, given its good performance. As shown in Fig. S7 in the ESM, the uranium concentration in solution remained constant without catalyst additives under stirring-light irradiation. In contrast, when $CdS@BaTiO_3$ was introduced, magnetic stirring led to a rapid decrease in U(VI) concentration. As the stirring speed increased from 500 to 2500 rpm (Fig. S8 in the ESM), U(VI) extraction efficiency increased from 40% to 99% during 150 min, corresponding reaction rates were 0.002, 0.016, and 0.040 min^{-1}. The stirring-driven efficiency (2500 rpm) for mechanical-to-chemical energy conversion was ~ 1.50%, as calculated based on Eqs. (S4)–(S7) in the ESM [43]. It is evident that stirring speed affected magnetic stir bar-water interfacial interaction, the turbulence and vortices generated during stirring act as mechanical force to induce a piezoelectric field [44]. Increasing stirring rate is expected to enhance solution vortex intensity and mass transfer efficiency [45, 46]. Moreover, according to the piezoelectric effect theory and Newton's law of viscosity, higher stirring speeds strengthen the built-in electric field within the system, and correspondingly increase the stress exerted on the catalyst surface [20, 47]. When irradiation was applied, U(VI) concentration declined rapidly, achieving a 98% decrease within 30 min (Fig. 4(b)). Obviously, the photocatalysis exhibits higher efficiency than piezocatalysis, likely due to the limited generation of free charge carriers under stirring alone. Compared to the individual systems, the coupling of piezocatalysis and photocatalysis yielded a markedly enhanced U(VI) separation efficiency, reaching over 98% recovery within only 10 min. The k values of $CdS@BaTiO_3$ are 0.331 min^{-1} (stirring + light), 0.132 min^{-1} (light), and 0.040 min^{-1} (stirring), respectively (Fig. 4(c)). Comparatively, the $CdS@BaTiO_3$ exhibited faster uranium separation rate than pure $BaTiO_3$, likely due to its more efficient charge carrier separation (Fig. S9 in the ESM). It was noteworthy that ultrasonic excitation resulted in a lower uranium separation efficiency than mechanical stirring (Fig. S10 in the ESM), reflecting the weaker drive provided by the former in promoting the separation process and reaction rate. Significantly, compared with recent studies (Fig. 4(e) and Table S1 in the ESM), the $CdS@BaTiO_3$ catalyst shows exceptional catalytic efficiency for uranium separation [37, 48–57]. Such pronounced enhancement verifies the synergistic coupling between the piezoelectric and photoelectric fields, which facilitates piezo-induced polarization, accelerates carrier separation, and thus boosts photocatalytic performance.

Under continuous operation, $CdS@BaTiO_3$ exhibits remarkable uranium separation capability, achieving a high capacity of 1893.2 $mg \cdot g^{-1}$ in piezo-photocatalytic conditions (Fig. S11 in the ESM). The gradual decline in uranium separation efficiency is

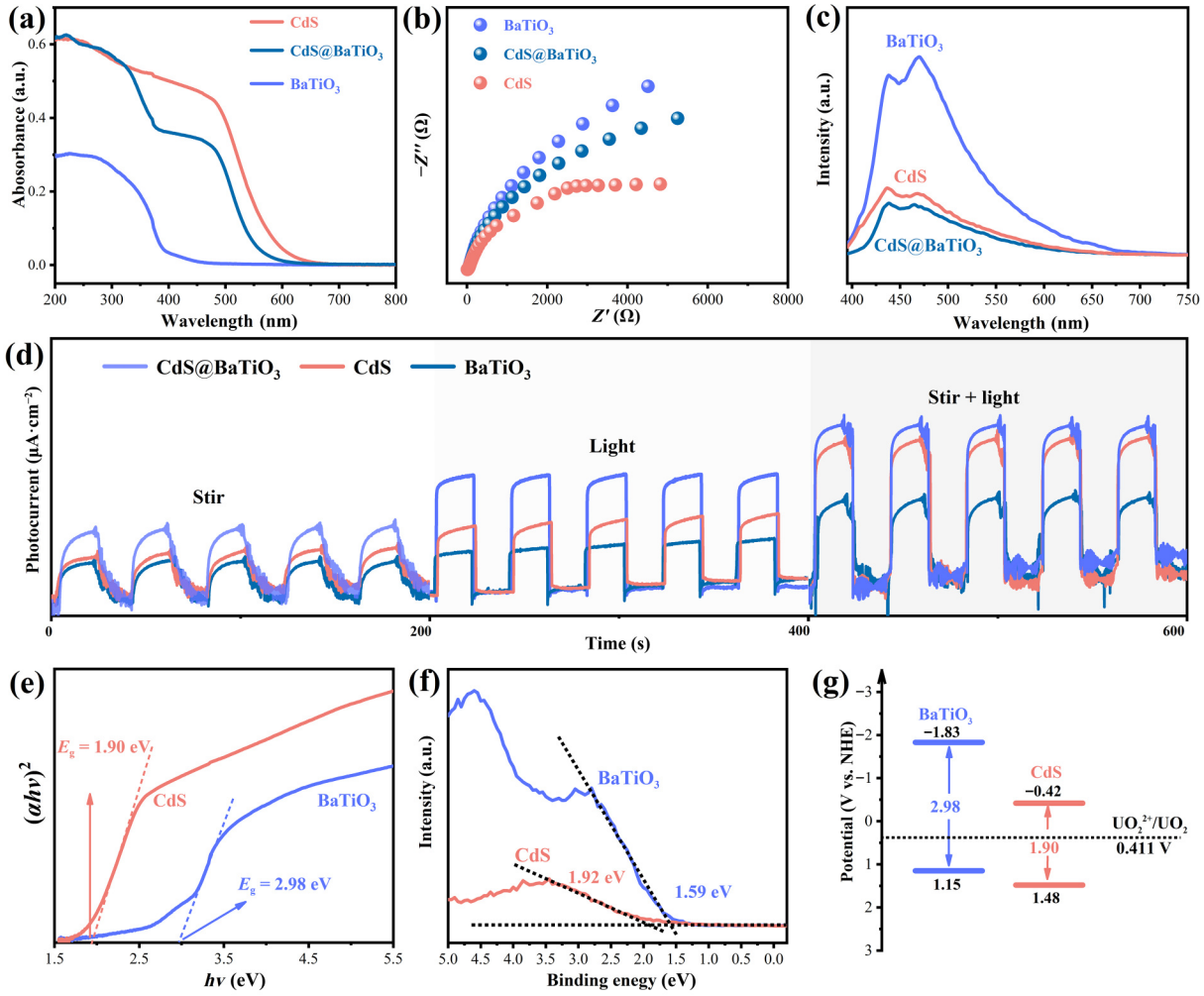


Figure 3 (a) DRS spectra, (b) EIS Nyquist plots, (c) PL spectra, and (d) transient photocurrent responses of CdS, $BaTiO_3$, and CdS@$BaTiO_3$. (e) Tauc plots, (f) valence band XPS spectra of CdS and $BaTiO_3$, and (g) schematic band position of CdS and $BaTiO_3$ catalysts.

plausibly due to uranium blocking the reactive sites or accumulating atop $BaTiO_3$, thereby limiting catalytic performance. Moreover, Na_2CO_3 solution allowed for faster and easier desorption for their good recyclability (Fig. S12 in the ESM). The uranium removal efficiency showed a slight decrease after four cycles, but still achieved ~ 80% in the final test (Fig. 4(d)). Partial loss of catalyst during the recovery process is inevitable, which may result in reduced catalytic activity and reaction efficiency. In addition, CdS@$BaTiO_3$ can effectively and selectively extract U(VI) with minimal interference from competing ions (Fig. S13 in the ESM). Meanwhile, XRD patterns and TEM image (Fig. S14 in the ESM) further verify the structural integrity of the recovered CdS@$BaTiO_3$, demonstrating the retention of both crystallinity and chemical stability.

3.4 Piezo-photocatalytic mechanisms

To further clarify the mechanism of uranium removal by CdS@$BaTiO_3$, the piezo-photocatalytic products were systematically characterized. The U 4f XPS spectrum (Fig. 5(a)) illustrates four main characteristic peaks at 381.4, 392.2, 380.2, and 391.2 eV, corresponding to U(VI) and U(IV), respectively, suggesting their coexistence after the piezo-photocatalytic reaction [58]. Besides, a lot of nanosized particles (Fig. 5(b)) appeared on material surface, indicating the formation of newly generated uranium-containing species. X-ray diffraction analysis (Fig. 5(c)) further revealed new diffraction peaks corresponding to UO_2 (PDF#01-073-2293) and metaschoepite ($((UO_2)_8O_2(OH)_{12}(H_2O)_{10}$, PDF#01-089-7333). Since no distinct diffraction peaks were observed under adsorption-only conditions (Fig. S15 in the ESM), it can be inferred that metaschoepite is not a direct product of initial uptake but rather evolved from the catalytic process. According to previous studies, the reduced UO_2 is thermodynamically unstable in aqueous environments and susceptible to gradual oxidative corrosion [59, 60]. During this transformation, U(IV) tends to be partially reoxidized to U(VI), followed by hydrolysis and condensation reactions, ultimately resulting in the formation of metaschoepite. Dark-field image and energy dispersive spectroscopy (EDS) mappings (Fig. 5(d)) further confirmed the immobilization of uranium, showing a uniform distribution of U on the catalyst surface. The strong spatial correlation between U and Cd signals demonstrates a directional electron transfer from $BaTiO_3$ to CdS, with significant electron accumulation at the CdS interface subsequently driving the reduction reaction, consistent with the Type-II charge-transfer pathway [1]. Furthermore, Figs. 5(e) and 5(f) exhibit a lattice spacing of 0.317 nm corresponding to the (111) plane of UO_2, providing additional evidence of U(IV) formation

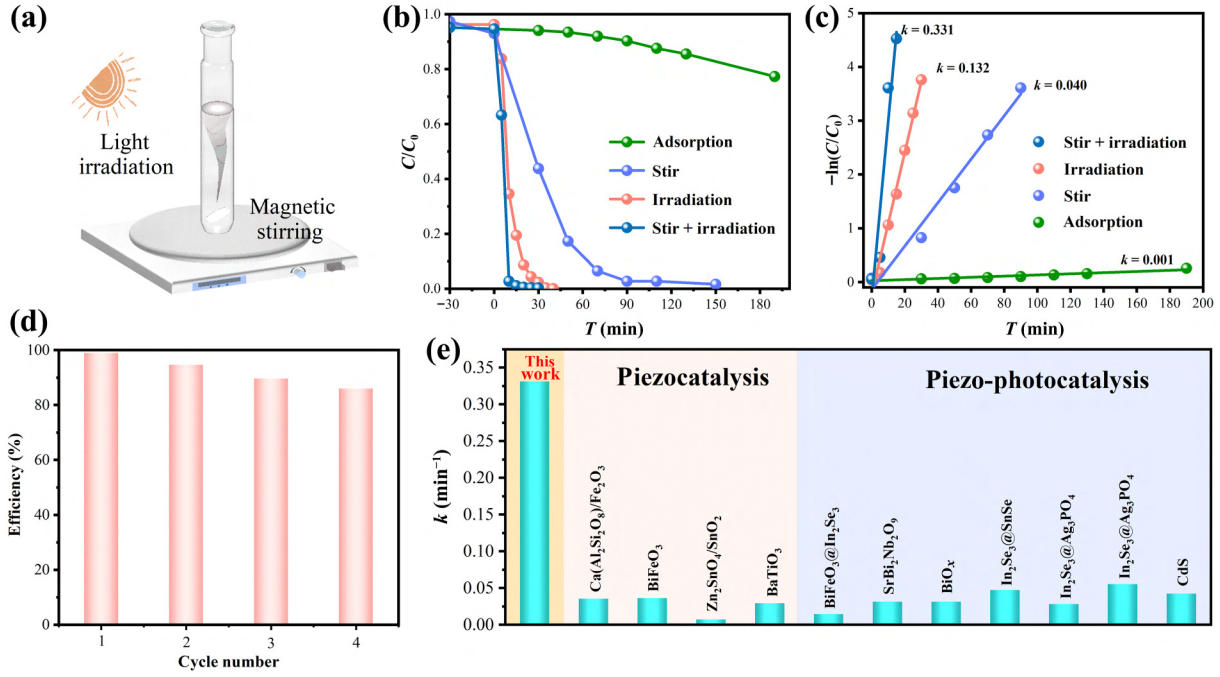


Figure 4 (a) The piezo-photocatalytic U(VI) experiment setup. (b) The U(VI) removal performance of CdS@$BaTiO_3$ and (c) corresponding pseudo-first-order kinetic fittings. (d) Cycling performance of CdS@$BaTiO_3$. (e) The comparison of the rate constants (k) for piezocatalytic and piezo-photocatalytic U(VI) reactions.

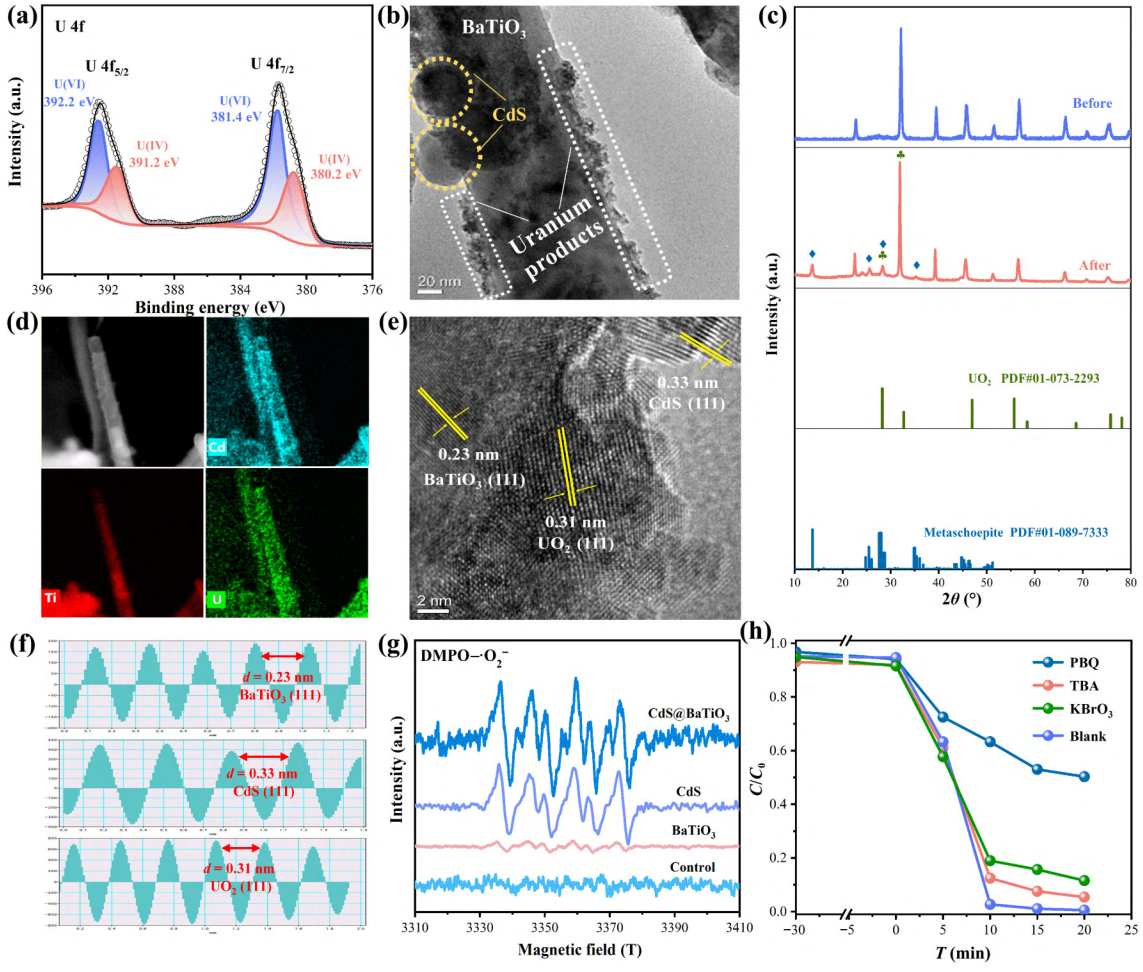


Figure 5 (a) XPS spectrum, (b) TEM image, and (c) XRD patterns of CdS@$BaTiO_3$ after piezo-photocatalytic reduction of U(VI). (d) Dark-field image of CdS@$BaTiO_3$ and EDS elemental mappings of Cd, Ti, and U. (e) HRTEM image and (f) lattice spacing measurement analysis of reaction products. (g) EPR spectra of ·DMPO–·O_2^- under light and stirring conditions. (h) Effects of radical scavengers on piezo-photocatalytic U(VI) removal by CdS@$BaTiO_3$.

during the piezo-photocatalytic process. Alternatively, the uranium products obtained under stirring alone are congruent with those produced in the coupled stirring-light process (Fig. S16 in the ESM). Light irradiation produces a significant synergistic enhancement with the piezoelectric effect without altering the reaction pathway, further accelerating the reduction rate (Fig. 4(c)). This demonstrates the kinetic superiority of the system in multi-field coupled catalysis.

The role of reactive species during uranium removal was further investigated. As shown in Fig. 5(g) and Fig. S17 in the ESM, characteristic electron spin resonance (EPR) signals corresponding to DMPO–·OH (DMPO: 5,5-dimethyl-1-pyrroline N-oxide) and DMPO–·O_2^- (·O_2^-: superoxide radicals) adducts were detected. Notably, much stronger peaks appeared in the CdS@$BaTiO_3$ heterojunction, evidencing that the piezo-photocatalytic synergistic coupling within the heterojunction maximizes the separation of photogenerated carriers, thus effectively enhancing piezo-photocatalytic efficiency. Moreover, CdS contributes more significantly to the piezoelectric and photocatalytic activity. Free radical trapping experiments were further conducted by using p-benzoquinone (p-BQ), potassium bromate ($KBrO_3$), and tert-butyl alcohol (TBA) as sacrificial agents of ·O_2^-, e^-, and ·OH, respectively. Specifically, TBA and $KBrO_3$ exhibited minor inhibition effect, implying that e^- and ·OH were not the dominant active species (Fig. 5(h)). In comparison, the addition of p-BQ induced evident inhibition of uranium removal efficiency, resulting in only 49.5% U(VI) removal, highlighting the essential involvement of ·O_2^- in the piezo-photocatalytic system. Similar trends were also observed under individual photocatalytic (Fig. S18 in the ESM) and piezoelectric (Fig. S19 in the ESM) experiments, indicating that ·O_2^- is the primary reactive oxygen species in mediating U(VI) reduction.

Based on the above findings, the piezo-photocatalytic mechanism of CdS@$BaTiO_3$ for uranium reduction can be inferred (Fig. 6). Under light irradiation, both $BaTiO_3$ and CdS are excited to produce electrons and holes. Driven by the IEF at Type-II heterojunction interface, photogenerated electrons migrate from the CB of $BaTiO_3$ to the CB of CdS, where they react with oxygen to form ·O_2^- (−0.33 eV vs. NHE) that participate in uranium reduction. When stirring is further introduced, the shear force of the fluid flow induces piezoelectric polarization within both $BaTiO_3$ and CdS, inducing energy band bending. This polarization drives negative electrons and positive holes toward higher and lower potential regions, respectively, tilting the CB and VB until a new equilibrium is established [61, 62]. Subsequently, the electrons recombine with those from $BaTiO_3$, driven by the IEF, reducing O_2 to ·O_2^-. The resulting ·O_2^- ultimately endows excellent piezo-photocatalytic performance for uranium separation [63]. Synergistic internal electric fields, generated through piezoelectric polarization and heterojunction formation, significantly promote the migration of photogenerated carriers and maximize interfacial charge separation. Notably, S-scheme heterojunctions involve selective recombination of low-energy electrons and holes at the interface, retaining only high-energy carriers for redox reactions, while Z-scheme heterojunctions rely on interfacial recombination to preserve strong redox potentials. Such recombination-dominated pathways or reversed charge-transfer behaviors are not observed in our system, further supporting the Type-II mechanism. The reaction pathways can be represented by the following equations

$$CdS + h\nu \rightarrow CdS(e^- + h^+) \quad (1)$$

$$BaTiO_3 + h\nu \rightarrow BaTiO_3(e^- + h^+) \quad (2)$$

$$UO_2^{2+} + 2e^- \rightarrow UO_2(s) \quad (3)$$

$$O_2 + e^- \rightarrow {}^{\cdot}O_2^- \quad (4)$$

$$UO_2^{2+} + 2\,{}^{\cdot}O_2^- \rightarrow UO_2(s) + 2O_2 \quad (5)$$

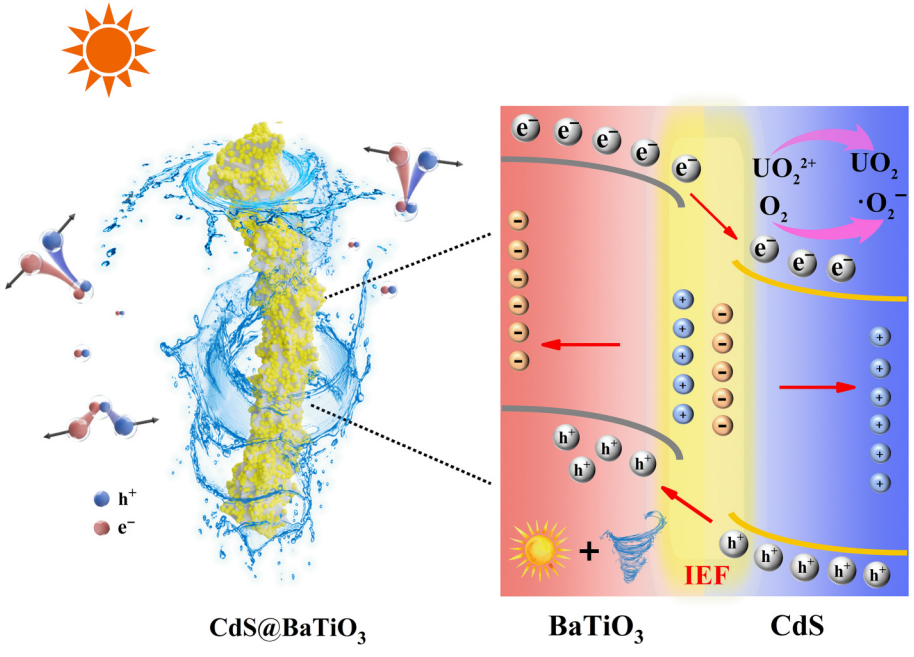


Figure 6 Schematic diagram of possible reaction mechanism for piezo-photocatalytic uranium removal over CdS@$BaTiO_3$ heterojunction.

4 Conclusions

In summary, a Type-II CdS@$BaTiO_3$ piezo-photocatalyst was successfully constructed, enabling efficient uranium extraction under light irradiation coupled with water-flow-driven mechanical stimulation. The heterojunction catalyst achieved a rapid U(VI) removal efficiency of 98% within 10 min, demonstrating significantly enhanced activity compared with photocatalysis and piezocatalysis alone. Notably, under continuous operation, CdS@$BaTiO_3$ exhibited a high uranium separation capacity of 1893.2 $mg \cdot g^{-1}$, highlighting its exceptional performance. The formation of a Type-II interface generated a built-in electric field that facilitated directional electron transfer from $BaTiO_3$ to CdS, whereas mechanical stirring induced strong piezoelectric polarization that further accelerated charge separation and migration. These dual effects promoted the generation of $\cdot O_2^-$ species, which dominated the reduction of U(VI) to UO_2 species. This work offers a promising pathway toward highly efficient and easily implementable uranium separation technologies.

Electronic Supplementary Material: Supplementary material (details of material characterization, photoelectric and electrochemical measurements, and additional supporting figures) is available in the online version of this article at https://doi.org/10.26599/NR.2026.94908657.

Data availability

All data needed to support the conclusions in the paper are presented in the manuscript and the Electronic Supplementary Material. Additional data related to this paper may be requested from the corresponding author upon request.

Acknowledgements

This work was financially supported by the National Natural Science Foundation of China (Nos. 22476211 and 22406147).

Declaration of competing interest

All the contributing authors report no conflict of interests in this work.

Author contribution statement

T. H.: Writing – original draft, investigation, validation, methodology. Y. X. J.: Methodology, data curation. W. W.: Validation. J. J. W.: Writing – review & editing, funding acquisition. P. L. (Peng Liu): Methodology, formal analysis. P. L. (Ping Li): Writing – review & editing, resources, funding acquisition. D. Q. P.: Supervision, methodology. Q. H. F.: Resources, project administration. All the authors have approved the final manuscript.

Use of AI statement

None.

References

[1] Li, P.; Wang, J. J.; Wang, Y.; Dong, L.; Wang, W.; Geng, R. Y.; Ding, Z.; Luo, D. X.; Pan, D. Q.; Liang, J. J. et al. Ultrafast recovery of aqueous uranium: Photocatalytic U(VI) reduction over CdS/g-C_3N_4. *Chem. Eng. J.* **2021**, *425*, 131552.

[2] Sun, Z. L.; Liao, Y.; Zhang, Y. Y.; Sun, S. R.; Kan, Q. H.; Wu, Z. Y.; Yu, L.; Dong, Z. M.; Wang, Z.; He, R. et al. Sustainable carbon materials in environmental and energy applications. *Sustainable Carbon Mater.* **2025**, *1*, e007.

[3] Chen, T.; Yu, K. F.; Dong, C. X.; Yuan, X.; Gong, X.; Lian, J.; Cao, X.; Li, M. Z.; Zhou, L.; Hu, B. W. et al. Advanced photocatalysts for uranium extraction: Elaborate design and future perspectives. *Coord. Chem. Rev.* **2022**, *467*, 214615.

[4] Sun, Z. L.; Chen, Z. S.; Tai, X. S.; Wang, X. K. Uranium extraction from seawater: Methods and challenges. *Sci. China Chem.* **2025**, *68*, 3923–3926.

[5] Wei, G.; Chen, Z. S.; Tai, X. S.; Sun, Z. L.; Wang, X. K. Recent progress of uranium extraction and its catalytic applications. *Trans. Tianjin Univ.* **2025**, *31*, 390–402.

[6] Ma, Y.; Gan, C.; Liu, L.; Pan, J. J.; Rong, H. Z.; Guo, Y.; Yuan, Y. H.; Wang, N. Polarization-π strategy for modulating excited-state band structures of covalent organic frameworks to enhance photocatalytic uranium extraction. *Adv. Funct. Mater.* **2026**, *36*, e23125.

[7] Huang, X. Y.; Yuan, X.; Xue, X. G.; Hong, C. X.; Huang, C. W.; Chen, M.; Zhang, B. W.; Song, Y.; Li, Z. M.; Chen, S. S. et al. Fabric-based dot-in-caged $AgInS_2$@CdS heterojunction for highly efficient photocatalytic uranium extraction via reductive crystallization. *Adv. Funct. Mater.* **2026**, *36*, e13087.

[8] Ghosh, D.; Maity, S.; Rasaily, S.; Roy, A.; Biswas, K.; Dam, G. K.; Ghosh, S. K. Enhancing photocatalytic activity of porous organic frameworks via facile post-synthetic modification for ultrafast uranium extraction. *Adv. Funct. Mater.* **2026**, *36*, e19249.

[9] Sheng, Y. Q.; Li, W. L.; Xu, L. L.; Zhu, Y. F. High photocatalytic oxygen evolution via strong built-in electric field induced by high crystallinity of perylene imide supramolecule. *Adv. Mater.* **2022**, *34*, 2102354.

[10] Qi, J. X.; Gong, J. W.; Zhang, C. R.; Peng, Z. H.; Cai, Y. J.; Liu, X.; Liu, J. L.; Chen, X. J.; Liang, R. R.; Qiu, J. D. Ocean wave-driven covalent organic framework/ZnO heterostructure composites for piezocatalytic uranium extraction from seawater. *Nat. Commun.* **2025**, *16*, 1078.

[11] Zheng, H. J.; Wang, Y. L.; Liu, J. S.; Wang, J.; Yan, K.; Zhu, K. J. Recent advancements in the use of novel piezoelectric materials for piezocatalytic and piezo-photocatalytic applications. *Appl. Catal. B: Environ.* **2024**, *341*, 123335.

[12] Lu, Y. C.; Hao, C. L.; Gao, S. S.; Zhao, X.; An, X. G.; Hu, G. Z. Piezoelectric catalysts for water pollutant remediation: Achievements, challenges, and perspectives. *Mater. Today.* **2025**, *88*, 415–440.

[13] Lv, H.; Liu, Y. N.; Zhao, P.; Bai, Y. B.; Cui, W. X.; Shen, S. L.; Liu, Y.; Wang, Z.; Yu, D. G. Insight into the superior piezophotocatalytic performance of $BaTiO_3$//ZnO Janus nanofibrous heterostructures in the treatment of multi-pollutants from water. *Appl. Catal. B: Environ.* **2023**, *330*, 122623.

[14] Lee, Y. J.; Chong, W. K.; Putri, L. K.; Ng, B. J.; Tan, L. L.; Wu, T. Y.; Chai, S. P. Complementary conjugated piezo-phototronic polarized blue TiO_2-KNN for piezophotocatalytic degradation of tetracycline enhanced under gentle oscillatory hydrodynamic disturbances. *Appl. Catal. B: Environ.* **2023**, *334*, 122836.

[15] Meng, N.; Liu, W.; Jiang, R. Y.; Zhang, Y.; Dunn, S.; Wu, J. Y.; Yan, H. X. Fundamentals, advances and perspectives of piezocatalysis: A marriage of solid-state physics and catalytic chemistry. *Prog. Mater. Sci.* **2023**, *138*, 101161.

[16] Tong, W. S.; Zhang, Y. H.; Huang, H. W.; Xiao, K.; Yu, S. X.; Zhou, Y.; Liu, L. P.; Li, H. T.; Liu, L.; Huang, T. et al. A highly sensitive hybridized soft piezophotocatalyst driven by gentle mechanical disturbances in water. *Nano Energy* **2018**, *53*, 513–523.

[17] Nie, G.; Hu, K. S.; Ren, W.; Zhou, P.; Duan, X. G.; Xiao, L.; Wang, S. B. Mechanical agitation accelerated ultrasonication for wastewater treatment: Sustainable production of hydroxyl radicals. *Water Res.* **2021**, *198*, 117124.

[18] Wang, K. Q.; Guan, Z. Y.; He, Y. M.; Fan, M. H. Harnessing zinc stannate for sustainable energy and environment solutions: Advances in photocatalytic, piezocatalytic, and piezo-photocatalytic technologies. *Nano Energy* **2025**, *133*, 110518.
[19] Pan, L.; Sun, S. C.; Chen, Y.; Wang, P. H.; Wang, J. Y.; Zhang, X. W.; Zou, J. J.; Wang, Z. L. Advances in piezo-phototronic effect enhanced photocatalysis and photoelectrocatalysis. *Adv. Energy Mater.* **2020**, *10*, 2000214.
[20] Feng, Y. M.; Ling, L. L.; Wang, Y. X.; Xu, Z. M.; Cao, F. L.; Li, H. X.; Bian, Z. F. Engineering spherical lead zirconate titanate to explore the essence of piezo-catalysis. *Nano Energy* **2017**, *40*, 481–486.
[21] Liu, J. Z.; Jin, L. J.; Dai, Z. Q.; Ji, Y. J.; Qian, J.; Lu, Y.; Wang, J.; Shen, B.; Li, Y. Y.; Xu, R. et al. Single atom embedding enhanced macroscopic polarization in carbon nitride nanosheets for pH-universal piezo-photocatalytic nitrate reduction over a wide concentration range. *ACS Catal.* **2025**, *15*, 4025–4038.
[22] Zhou, J. X.; Chen, W. R.; Chen, Q.; Li, X. K.; Wang, J.; Liao, G. Z.; Li, L. S. Construction of $BaTiO_3$/g-C_3N_4 heterojunction for promoting atrazine degradation of hydraulic-driven piezocatalytic ozonation. *Appl. Catal. B: Environ.* **2025**, *362*, 124702.
[23] Zhang, Q. C.; Jia, Y. M.; Wu, W. W.; Pei, C. J.; Zhu, G. Q.; Wu, Z. S.; Zhang, L. H.; Fan, W.; Wu, Z. Review on strategies toward efficient piezocatalysis of $BaTiO_3$ nanomaterials for wastewater treatment through harvesting vibration energy. *Nano Energy* **2023**, *113*, 108507.
[24] Xu, S. Y.; Guo, L. M.; Sun, Q. J.; Wang, Z. L. Piezotronic effect enhanced plasmonic photocatalysis by AuNPs/$BaTiO_3$ heterostructures. *Adv. Funct. Mater.* **2019**, *29*, 1808737.
[25] Lei, Y. Q.; Xu, S. Y.; Ding, M.; Li, L. L.; Sun, Q. J.; Wang, Z. L. Enhanced photocatalysis by synergistic piezotronic effect and exciton-Plasmon interaction based on (Ag–Ag_2S)/$BaTiO_3$ heterostructures. *Adv. Funct. Mater.* **2020**, *30*, 2005716.
[26] Zhang, M. Y.; Nie, S. Y.; Cheng, T.; Feng, Y.; Zhang, C. C.; Zheng, L.; Wu, L.; Hao, W. C.; Ding, Y. Enhancing the macroscopic polarization of CdS for piezo-photocatalytic water splitting. *Nano Energy* **2021**, *90*, 106635.
[27] Huang, X. Y.; Lei, R.; Yuan, J.; Gao, F.; Jiang, C. K.; Feng, W. H.; Zhuang, J. D.; Liu, P. Insight into the piezo-photo coupling effect of $PbTiO_3$/CdS composites for piezo-photocatalytic hydrogen production. *Appl. Catal. B: Environ.* **2021**, *282*, 119586.
[28] Low, J.; Yu, J. G.; Jaroniec, M.; Wageh, S.; Al-Ghamdi, A. A. Heterojunction photocatalysts. *Adv. Mater.* **2017**, *29*, 1601694.
[29] Liu, W.; Wang, P. F.; Ao, Y. H.; Chen, J.; Gao, X.; Jia, B. H.; Ma, T. Y. Directing charge transfer in a chemical-bonded $BaTiO_3$@ReS_2 Schottky heterojunction for piezoelectric enhanced photocatalysis. *Adv. Mater.* **2022**, *34*, 2202508.
[30] Fan, F. R.; Tang, W.; Wang, Z. L. Flexible nanogenerators for energy harvesting and self-powered electronics. *Adv. Mater.* **2016**, *28*, 4283–4305.
[31] Zhao, X. N.; Lei, Y. C.; Fang, P. F.; Li, H. J.; Han, Q.; Hu, W. G.; He, C. Q. Piezotronic effect of single/few-layers MoS_2 nanosheets composite with TiO_2 nanorod heterojunction. *Nano Energy* **2019**, *66*, 104168.
[32] Pei, H. N.; Dong, Z. M.; Li, Z. F.; Huang, J.; Jiang, Y. P.; Li, Z. J.; Xu, L.; Cao, X. H.; Liu, Y. H.; Zhang, Z. B. et al. Synergistic effect of homojunction and Ohmic junctions in CdS boosting spatial charge separation for U(VI) photoreduction. *Nano Res.* **2024**, *17*, 6849–6859.
[33] Li, W. L.; Zheng, X. H.; Xu, B. B.; Yang, Y.; Zhang, Y. F.; Cai, L. C.; Wang, Z. J.; Yao, Y. F.; Nan, B.; Li, L. N. et al. Atomic ruthenium-promoted cadmium sulfide for photocatalytic production of amino acids from biomass derivatives. *Angew. Chem., Int. Ed.* **2024**, *63*, e202320014.
[34] Han, G. Q.; Jin, Y. H.; Burgess, R. A.; Dickenson, N. E.; Cao, X. M.; Sun, Y. J. Visible-light-driven valorization of biomass intermediates integrated with H_2 production catalyzed by ultrathin Ni/CdS nanosheets. *J. Am. Chem. Soc.* **2017**, *139*, 15584–15587.
[35] Zhu, C.; Liu, C.; Fu, Y. J.; Gao, J.; Huang, H.; Liu, Y.; Kang, Z. H. Construction of CDs/CdS photocatalysts for stable and efficient hydrogen production in water and seawater. *Appl. Catal. B: Environ.* **2019**, *242*, 178–185.
[36] Liu, X. L.; Dai, D. J.; Cui, Z. H.; Zhang, Q. Q.; Gong, X. Q.; Wang, Z. Y.; Liu, Y. Y.; Zheng, Z. K.; Cheng, H. F.; Dai, Y. et al. Optimizing the reaction pathway by active site regulation in the CdS/Fe_2O_3 Z-scheme heterojunction system for highly selective photocatalytic benzylamine oxidation integrated with H_2 production. *ACS Catal.* **2022**, *12*, 12386–12397.
[37] Guo, R. S.; Jin, L. H.; Wang, H. Q.; Wang, R. B.; Zhang, X. Y.; Zhang, Y. High-efficient U(VI) removal from organic wastewater through polarization electric field enhanced photocatalysis with In_2Se_3@Ag_3PO_4 heterojunction. *J. Water Process Eng.* **2025**, *69*, 106690.
[38] Zhang, Y. C.; Ma, Q.; Zhang, H.; Chen, Z. S.; Wang, X. X.; Lin, Z. M.; Xu, F. Y.; Shao, H. X.; Zhang, F. F.; Fu, D. et al. Iodine doping covalent organic frameworks to reduce electron–hole recombination for promoting photocatalytic performance. *Sci. Bull.* **2026**, *71*, 388–398.
[39] Fu, Y. M.; Ren, Z. Q.; Wu, J. Z.; Li, Y. Q.; Liu, W. L.; Li, P.; Xing, L. L.; Ma, J.; Wang, H.; Xue, X. Y. Direct Z-scheme heterojunction of ZnO/MoS_2 nanoarrays realized by flowing-induced piezoelectric field for enhanced sunlight photocatalytic performances. *Appl. Catal. B: Environ.* **2021**, *285*, 119785.
[40] Yu, C.; He, J.; Lan, S. Y.; Guo, W. Q.; Zhu, M. S. Enhanced utilization efficiency of peroxymonosulfate via water vortex-driven piezo-activation for removing organic contaminants from water. *Environ. Sci. Ecotechnol.* **2022**, *10*, 100165.
[41] Feng, Y. W.; Li, H.; Ling, L. L.; Yan, S.; Pan, D. L.; Ge, H.; Li, H. X.; Bian, Z. F. Enhanced photocatalytic degradation performance by fluid-induced piezoelectric field. *Environ. Sci. Technol.* **2018**, *52*, 7842–7848.
[42] Deng, X. X.; Wang, Y.; Zhang, J. W.; Gong, X. Y.; Cui, R. R.; Chen, P.; Deng, C. Y. Synergistically triggering macroscopic polarization and dynamic reconfiguration of CdS@SnS_2 heterojunction to enhance piezo-photocatalytic nitrate reduction. *Compos. B: Eng.* **2025**, *293*, 112108.
[43] Hu, P. H.; Xu, Y.; Lei, Y. H.; Yuan, J.; Lei, R.; Hu, R.; Chen, J. K.; Xu, D. F.; Zhang, S. Y.; Liu, P. et al. Piezoelectric nanofoams with the interlaced ultrathin graphene confining Zn–N–C dipoles for efficient piezocatalytic H_2 evolution under low-frequency vibration. *J. Energy Chem.* **2022**, *69*, 115–122.
[44] Chen, X. Y.; Liu, L. F.; Feng, Y. W.; Wang, L. F.; Bian, Z. F.; Li, H. X.; Wang, Z. L. Fluid eddy induced piezo-promoted photodegradation of organic dye pollutants in wastewater on ZnO nanorod arrays/3D Ni foam. *Mater Today.* **2017**, *20*, 501–506.
[45] Candel, S. M. Numerical solution of wave scattering problems in the parabolic approximation. *J. Fluid Mech.* **1979**, *90*, 465–507.
[46] Zhang, X. G.; Hao, C. C.; Ma, C.; Shen, Z. Z.; Guo, J. Z.; Sun, R. G. Studied on sonocatalytic degradation of Rhodamine B in aqueous solution. *Ultrason. Sonochem.* **2019**, *58*, 104691.
[47] Tu, S. C.; Guo, Y. X.; Zhang, Y. H.; Hu, C.; Zhang, T. R.; Ma, T. Y.; Huang, H. W. Piezocatalysis and piezo-photocatalysis: Catalysts classification and modification strategy, reaction mechanism, and practical application. *Adv. Funct. Mater.* **2020**, *30*, 2005158.
[48] Guo, R. S.; Jin, L. H.; Zhang, Y. Piezo-catalysis in $BiFeO_3$@In_2Se_3 heterojunction for high-efficiency uranium removal. *Small* **2024**, *20*, 2307946.
[49] Liu, B. Y.; Gao, F. X.; Zhang, S.; Fang, M.; Yu, L.; Tan, X. L.; Ni, M. Y. Boosted charge transfer in a naturally formed $Ca(Al_2Si_2O_8)$/Fe_2O_3 heterojunction for piezocatalytical formation of H_2O_2 and solidification of U(VI). *J. Colloid Interface Sci.* **2024**, *667*, 575–584.
[50] Guo, R. S.; Zhang, X. Y.; Chen, Y. X.; Zhang, Y. Internal electric

field-induced high-efficiency piezo-photocatalytic performance in bimetal-regulated layered perovskite $SrBi_2Nb_2O_9$. *Adv. Funct. Mater.* **2024**, *34*, 2408838.

[51] Guo, R. S.; Jin, L. H.; Zhang, X. Y.; Zhang, Y. Bimetal doping enhanced polarization electric field in $BiFeO_3$ for piezocatalytic U(VI) reduction and hydrogen production. *Appl. Catal. B: Environ. Energy* **2025**, *367*, 125113.

[52] Cai, Y. W.; Zhang, Y. F.; Lv, Z. M.; Zhang, S.; Gao, F. X.; Fang, M.; Kong, M. G.; Liu, P. S.; Tan, X. L.; Hu, B. W. et al. Highly efficient uranium extraction by a piezo catalytic reduction-oxidation process. *Appl. Catal. B: Environ.* **2022**, *310*, 121343.

[53] Gao, D. L.; Dong, Z. M.; Feng, W. L.; Li, Z. F.; Wu, H. T.; Wu, Y. X.; Wei, Q. L.; Meng, C.; Wu, Y. C.; Wang, Y. Q. et al. Dipole moment and built-in polarization electric field induced by oxygen vacancies in BiOX for boosting piezoelectric-photocatalytic removal of uranium(VI). *Inorg. Chem.* **2024**, *63*, 5931–5944.

[54] Guo, R. S.; Jin, L. H.; Chen, Y. X.; Zhang, X. Y.; Zhang, Y. Piezo-photocatalysis of S-scheme In_2Se_3@SnSe heterojunctions for highly efficient U(VI) removal and hydrogen production from organic wastewater. *J. Environ. Chem. Eng.* **2024**, *12*, 114304.

[55] Zhu, W. C.; Wang, C. T.; Hui, W. H.; Huang, X.; Yang, C. M.; Liang, Y. C. Intrinsically morphological effect of perovskite $BaTiO_3$ boosting piezocatalytic uranium extraction efficiency and mechanism investigation. *J. Hazard. Mater.* **2023**, *455*, 131578.

[56] Zhang, X. Y.; Chen, Y. X.; Guo, R. S.; Zhang, Z. J.; Sun, Z.; Zhang, Y.; Yan, F. Three birds with one stone: A piezo-photocatalytic system for synergistic environmental remediation through simultaneous ionic liquids degradation, H_2 production, and uranium reduction. *Appl. Catal. B: Environ.* **2025**, *372*, 125314.

[57] Dong, Z. M.; Gao, D. L.; Li, Z. F.; Pei, H. N.; Xu, L.; Huang, J.; Cao, X. C.; Wang, Y. Q.; Wang, T.; Wei, Q. L. et al. Harvesting the vibration energy of CdS for high-efficient piezo-photocatalysis removal of U(VI): Roles of shape dependent and piezoelectric polarization. *Energy Environ. Mater.* **2024**, *7*, e12705.

[58] Liu, X. L.; Xiao, M. L.; Yang, X. Y.; Wang, L.; Gu, H.; Xie, Y. H.; Hao, M. J.; Waterhouse, G. I. N.; Tai, X. S.; Yang, H. Construction of nanospace-confined adsorption electrocatalyst for efficient uranium extraction from fluoride-containing wastewater. *Sci. China Chem.* **2025**, *68*, 6503–6512.

[59] Li, P.; Wang, J. J.; Wang, Y.; Liang, J. J.; He, B. H.; Pan, D. Q.; Fan, Q. H.; Wang, X. K. Photoconversion of U(VI) by TiO_2: An efficient strategy for seawater uranium extraction. *Chem. Eng. J.* **2019**, *365*, 231–241.

[60] Ma, H. Y.; Wang, H. T.; Burns, P. C.; Mcnamara, B. K.; Buck, E. C.; Na, C. Synthesis and preservation of graphene-supported uranium dioxide nanocrystals. *J. Nucl. Mater.* **2016**, *475*, 113–122.

[61] Guo, L. N.; Hu, C.; Tu, S. C.; Wang, C. C.; Mei, L. F.; Zhang, Y. H.; Huang, H. W. Weak force-polarization driven exceptional piezo-photocatalysis by coupling dual-active piezoelectric semiconductors in $NaNbO_3$/g-C_3N_4 heterojunction. *Chem. Eng. J.* **2023**, *476*, 146541.

[62] Li, Y. R.; Zhang, X. L.; Sha, R.; Li, T.; Hu, C.; Tu, S. C.; Chen, F.; Huang, H. W. Efficient piezo-photocatalysis of $Bi_2O_2(OH)NO_3$/BiOI heterojunction: Collaboration of piezoelectric polarization and interface electric field. *Chem. Eng. J.* **2024**, *480*, 147976.

[63] Hu, C.; Tu, S. C.; Tian, N.; Ma, T. Y.; Zhang, Y. H.; Huang, H. W. Photocatalysis enhanced by external fields. *Angew. Chem., Int. Ed.* **2021**, *60*, 16309–16328.

This is an open access article under the terms of the Creative Commons Attribution 4.0 International License (CC BY 4.0, https://creativecommons.org/licenses/by/4.0/).

© The Author(s) 2026. Published by Tsinghua University Press.